Kinetic Analysis of Barium Currents in Chick Cochlear Hair Cells

Michael Zidanic and Paul A. Fuchs
Department of Physiology, University of Colorado Health Sciences Center, Denver, Colorado 80262 USA

ABSTRACT Inward barium current (I_{Ba}) through voltage-gated calcium channels was recorded from chick cochlear hair cells using the whole-cell clamp technique. I_{Ba} was sensitive to dihydropyridines and insensitive to the peptide toxins ω-agatoxin IVa, ω-conotoxin GVIa, and ω-conotoxin MVIIC. Changing the holding potential over a −40 to −80 mV range had no effect on the time course or magnitude of I_{Ba} nor did it reveal any inactivating inward currents. The activation of I_{Ba} was modeled with Hodgkin-Huxley m^2 kinetics. The time constant of activation, τ_m, was 550 μs at −30 mV and gradually decreased to 100 μs at +50 mV. A Boltzmann fit to the activation curve, m_∞, yielded a half activation voltage of −15 mV and a steepness factor of 7.8 mV. Opening and closing rate constants, α_m and β_m, were calculated from τ_m and m_∞, then fit with modified exponential functions. The H-H model derived by evaluating the exponential functions for α_m and β_m not only provided an excellent fit to the time course of I_{Ba} activation, but was predictive of the time course and magnitude of the I_{Ba} tail current. No differences in kinetics or voltage dependence of activation of I_{Ba} were found between tall and short hair cells. We conclude that both tall and short hair cells of the chick cochlea predominantly, if not exclusively, express noninactivating L-type calcium channels. These channels are therefore responsible for processes requiring voltage-dependent calcium entry through the basolateral cell membrane, such as transmitter release and activation of Ca^{2+}-dependent K^+ channels.

INTRODUCTION

A fundamental problem in auditory physiology is to understand the mechanisms that animals have evolved to hear sounds at very low levels and to perform fine frequency analysis of complex sounds. In mammals, an electromechanical feedback from the outer hair cells is thought to modify cochlear mechanics in such a way as to increase the sensitivity and sharpen the frequency selectivity of the traveling wave along the cochlear partition (Davis, 1985). In turtles (Crawford and Fettiplace, 1981) and frogs (Ashmore, 1983; Lewis and Hudspeth, 1983; Pitchford and Ashmore, 1987), where no such traveling wave exists, frequency selectivity is achieved by means of an electrical tuning mechanism intrinsic to the hair cell membrane.

In birds, preferred intervals in the spontaneous activity of auditory neurons corresponding to characteristic frequencies as high as 1.5 kHz (Manley et al., 1985; Manley, 1979) first suggested that the membrane potential of chick hair cells undergoes spontaneous oscillations in vivo. That the oscillations derive from electrical tuning is supported by the finding that isolated chick cochlear hair cells show ringing responses (Fuchs et al., 1988) similar to those described for frog and turtle hair cells. Even more compelling is the fact that the temperature dependence of the chick hair cell ringing response (Fuchs and Evans, 1990) is similar to that reported for the tuning of pigeon auditory nerve fibers (Schermuly and Klinke, 1985), i.e., characteristic frequency decreases one octave per 10°C reduction in temperature.

Received for publication 25 March 1994 and in final form 11 January 1995.

Address reprint requests to Michael Zidanic, Department of Physiology, University of Colorado Health Sciences Center, 4200 E. Ninth Avenue, C240, Denver, CO 80262. Tel.: 303-270-5007; Fax: 303-270-8110; E-mail: zidanicm@essex.hsc.colorado.edu.

0006-3495/95/04/1323/14 $2.00

Kinetic analysis of hair cell currents has revealed that electrical tuning can be explained by interactions between an inward Ca^{2+} current, I_{Ca}, and an outward Ca^{2+}-activated K^+ current, $I_{k(ca)}$ (Ashmore and Attwell, 1985; Art and Fettiplace, 1987; Hudspeth and Lewis, 1988a, b). The electrical tuning model put forth by Hudspeth and Lewis (1988b) was able to generate tuned responses for frequencies as high as 600 Hz. This frequency limit is well above the frequency range of vibrations sensed by the seismic receptors of the bullfrog sacculus (150 Hz) (Lewis et al., 1985), but is very close to the upper frequency limit of hearing in turtles (700 Hz) (Crawford and Fettiplace, 1980). If electrical tuning is responsible for the preferred intervals in avian auditory neurons, then either a qualitatively different mechanism is utilized or else the biophysical parameters of the model for chick hair cells must be very different from those of the bullfrog sacculus and turtle cochlea. In this paper we take our first step in building a biophysical model of chick hair cells by developing a Hodgkin-Huxley model of I_{Ca} using Ba^{2+} as charge carrier.

Hair cells of the avian cochlea can be broadly separated into two populations, tall and short. Tall cells are located on the neural edge of the epithelium, short hair cells on the abneural edge, with cells of intermediate height in between. The afferent and efferent innervation pattern of tall versus short cells (Takasaka and Smith, 1971; Tanaka and Smith, 1978; Hirokawa, 1978; Fischer, 1992) is reminiscent of that seen in the mammalian cochlea for inner and outer hair cells (Spoendlin, 1972), i.e., tall hair cells receive most of the afferent innervation (like the inner hair cells), whereas the short hair cells receive predominantly efferent innervation (like the outer hair cells).

A previous study in our laboratory described a Ca^{2+} current in chick cochlear hair cells (Fuchs et al., 1990) whose kinetic and pharmacological profile most closely matched the L-type class of calcium channels found elsewhere

(Nowycky et al., 1985; Fox et al., 1987). That study was limited to an examination of tall hair cells. In this study we characterize a similar Ca^{2+} current in short hair cells. We show that both tall and short hair cells of the chick cochlea express only a single type of noninactivating Ca^{2+} channel. These channels are therefore responsible for voltage-dependent processes requiring Ca^{2+} entry through the basolateral cell membrane, such as transmitter release and activation of $I_{k(ca)}$ for electrical tuning. A preliminary report of these results has been presented in abstract form (Zidanic and Fuchs, 1993).

MATERIALS AND METHODS

Hair cell dissociation

The procedures previously described for isolating chick cochlear hair cells (Fuchs et al., 1988) were slightly modified in this study to achieve a more rapid dissection of the cochlea. Briefly, 1–3 week old post-hatch Leghorn chicks of either sex were decapitated and the skull split along the sagittal midline. A smaller piece of bone containing the cochlea was obtained by making a transverse cut just anterior to the external auditory meatus and posterior to the eye. The smaller posterior portion of the skull was then placed in control saline solution (mM): 145 NaCl, 6 KCl, 4 $CaCl_2$, 1 $MgCl_2$, 10 glucose, 10 HEPES buffered to pH 7.35 with 4 NaOH, osmolarity 317 mOsm/kg. Further dissection was carried out under a dissecting microscope. The temporal bone was held with the anterior end facing up bringing the columella into view. The columella was removed and the soft tissue overlying the cochlea cleared to the apical tip of the cochlea. The whitish otoconia of the lagena that could be seen through the bone/cartilage provided an excellent landmark for the apical tip of the cochlea. The bone/cartilage surrounding the cochlea was carefully removed and then the cochlea with auditory nerve attached was finally removed from the temporal bone. In later experiments it was found easier to leave the bone/cartilage at the apical end of the cochlea intact. In this case, the cochlea was pulled out from the basal end which also conveniently separated the cochlea from the auditory nerve stump and provided improved optics of the neural half of the cochlea.

The tegmentum vasculosum was opened up with forceps and the cochlea transferred (using a broken back Pasteur pipette) to a Petri dish containing 0.01% endopeptidase (protease type XXIV, Sigma, St. Louis, MO) and 0.05% bovine albumin (BSA) in a low-divalent solution (mM): 145 NaCl, 6 KCl, 0.1 $CaCl_2$, 1 $MgCl_2$, 10 glucose, and 10 HEPES buffered to pH 7.35 with 4 NaOH. After 10 min in the enzyme solution, the cochlea was first rinsed in the low-divalent solution and 0.05% BSA solution, rinsed in control saline and 0.05% BSA, then placed in modified Eagle's medium (430–2800EB, GIBCO, Gaithersburg, MD) to which was added 3.7 g $NaHCO_3$ (final concentrations (mM): 1.8 $CaCl_2$, 5.4 KCl, 110 NaCl, 0.8 $MgSO_4$, 0.8 Na_2HPO_4, 44 $NaHCO_3$, and 25 D-glucose). The cochlea was secured to the bottom of a Sylgard-coated dish with miniature pins. A finely etched tungsten needle was used to detach the tectorial membrane from the apical end of the cochlea which was then peeled off the basilar papilla toward the basal end. The cochlea was then placed in an incubator (5% CO_2) at 37°C for 1–3 h before cells were isolated.

Cells located 0.9–1.0 mm from the apical tip were aspirated off the basilar papilla with a fire-polished pipette (tip opening ~30 μm) coated with Prosil-28 (PCR Inc., Gainesville, FL). A patch of cells ~50–150 μm across the width of the epithelium (total width ~370 μm at the 1.0 mm region) was transferred to the recording chamber containing control saline. The cochlea was returned to the incubator until another batch of cells was needed. The coverslip forming the bottom of the recording chamber was pretreated with control saline and 0.05% BSA so that cells would attach only loosely to the glass. Cells were viewed under an inverted microscope equipped with Hoffman contrast optics. Usually there were several isolated cells in each dish that appeared healthy (stereocilia intact, no Brownian motion of organelles, no swelling).

Whole cell recording

Patch pipettes were pulled on a vertical puller from borosilicate glass with bath resistance 2.3–3.5 MΩ and coated with cross-country ski wax (SWIX Sport A/X, Norway). Pipettes were filled with (in mM) 130 CsCl, 5 KCl, 2 $MgCl_2$, 5 Na_2ATP (added on the day of the experiment), 0.1 $CaCl_2$, 11 EGTA, 10 HEPES buffered to pH 7.2 with 34 CsOH, osmolarity 309 mOsm/kg). In later experiments (cells with CSb prefix), the 5 mM KCl was replaced with an additional 5 mM CsCl in an attempt to reduce residual outward K^+ currents. The total removal of K^+ from the internal solution had no obvious effect on either the Ca^{2+} or residual K^+ currents. Results are presented without correction for liquid junction potentials (−3 mV for the internal cesium solution). All experiments were carried out at room temperature (22–24°C). Seals in the range 1–5 GΩ were made with the cell bathed in control saline. The cell was lifted off the coverslip and the capacitance compensation controls on the patch clamp amplifier (model 3900 Dagan, Minneapolis, MN) were adjusted to minimize the charging transient. No series resistance compensation was used. Currents were filtered with the model 3900 internal 8-pole Bessel filter with a cutoff frequency of 10 kHz. Generation of command voltages and digitization of clamp current were under control of pCLAMP (Axon Instruments, Burlingame, CA) running on an 80286-based computer equipped with a 100-kHz analog-to-digital interface. Current gain was set at 10 mV/pA for a dynamic range of ±1 nA and resolution of 0.5 pA/A-D unit.

The interior of the pipette was held at either −80 or −60 mV and pulsed to 0 mV four times per second as the whole cell configuration was achieved. Subsequent pulses at one per second were continued for at least 30 s to allow for the exchange of the cell contents with the pipette solution. Series resistance, clamp speed, and membrane capacitance were measured by analyzing capacitive transients evoked by hyperpolarizing pulses from a holding potential of −60 mV (see Fig. 15 for details). Single exponential fits to the decay phase of capacitive transients indicated that the time constant of the voltage clamp (i.e., clamp speed) ranged from 27.5 to 133 μs ($n = 14$). Integration of capacitive transients revealed a mean membrane capacitance, C_m, of 7.4 ± 1.1 pF (range: 6.3–9.3 pF; standard deviations of the mean are presented here and elsewhere). Tall ($n = 8$) and short ($n = 6$) hair cells had mean membrane capacitances within 0.5 pF of each other. When the time constant was divided by C_m, the resulting series resistance ranged from 3.6 to 21 MΩ, representing a 2.8 ± 1.4 (range: 1.4–6.0)-fold increase in series resistance after achieving the whole-cell configuration. For all cells included in this study, the voltage error due to series resistance was less than 1.5 mV with respect to measurements of steady-state *I-V* curves.

Pharmacological experiments were performed by first exchanging control saline with a TEA-Ba solution (in mM: 20 $BaCl_2$, 140 TEACl, 1 $MgCl_2$, 10 HEPES buffered to pH 7.3 with 4 NaOH, osmolarity 298 mOsm/kg) to record control I_{Ba}. Bath exchange was achieved by first removing all but 150–200 μl of fluid in the center well of the recording chamber and then adding 2–3 ml of the exchange solution. Stock solutions of drugs were diluted into 2–3 ml TEA-Ba, which was then exchanged with TEA-Ba solution. Stock solutions (10 mM) of DHPs were made by dissolving into ethanol. Peptide toxins were dissolved in distilled water at 100 μM and stored as frozen aliquots. Drugs were obtained as follows: nifedipine and Bay K 8644 (Calbiochem, La Jolla, CA), nimodipine, nitrendipine, and ω-conotoxin MVIIC (RBI, Natick, MA), ω-conotoxin GVIA (Sigma, St. Louis, MO), ω-agatoxin IVa (gift from Pfizer, Inc., Groton, CT). The potency of ω-conotoxin GVIA was checked by its ability to completely block transmission at the frog neuromuscular junction within several minutes at a concentration of 1–3 μM.

For the kinetic experiments, a barium solution (in mM: 20 $BaCl_2$, 121 NaCl, 6 KCl, 1 $MgCl_2$, 10 HEPES buffered to pH 7.3 with 4 NaOH, osmolarity 305 mOsm/kg) was perfused onto the cell through a pipette (tip diameter 200 μm) located 100–300 μm from the cell. Leak subtracted currents were obtained using the pCLAMP P/4 protocol with hyperpolarizing prepulses. Two protocols were used to collect the data presented in results: 1) from a holding potential of −60 mV, *I-V* curves were obtained with 32.5 ms pulses over the −50 to +60 mV range and tail currents measured (over a 15 ms interval) upon repolarization to −60 mV (50 μs digitization rate), and 2) instantaneous *I-V* curves were obtained by following a −60 to 0 mV

test pulse (20 ms duration, 50 μs digitization rate) with a repolarizing pulse (5 ms duration) covering the −110 to −20 mV range (split clock rate changed to 10 μs upon repolarization for maximum resolution of tail current). Six to ten repetitions of each episode were averaged. Data files collected with pCLAMP were saved on disk then converted to MATLAB (The Mathworks, Inc., Natick, MA) format for subsequent analysis. After barium currents were recorded from a cell, the remaining cells and solution were discarded to avoid any lingering effects of the barium perfusion. Another batch of cells was then isolated and the recording process reiterated.

Hodgkin-Huxley model of I_{Ba}

Activation of the barium current, I_{Ba}, is described by a Hodgkin-Huxley (1952) model without inactivation:

$$i(t) = m^a g_{max}(V_m - E_r), \quad (1)$$

where g_{max} is the maximal conductance when all calcium channels are open, m is the voltage and time-dependent activation parameter with exponent of activation a, V_m is membrane potential, and E_r is the reversal potential. First order kinetics with voltage-dependent opening (α_m) and closing (β_m) rate constants are assumed for the transition between open and closed states:

$$\text{“}1 - m^n \underset{\beta_m}{\overset{\alpha_m}{\rightleftarrows}} m^n\text{”} \quad (2)$$

$$dm/dt = \alpha_m(1 - m) - \beta_m m. \quad (3)$$

For a step change in membrane potential, Eq. 3 can be solved by making the substitutions,

$$\tau_m = 1/(\alpha_m + \beta_m) \quad (4)$$

and

$$m_\infty = \alpha_m/(\alpha_m + \beta_m), \quad (5)$$

to derive the solution in the following form:

$$m(t) = m_\infty + (m_0 - m_\infty)\exp(-t/\tau_m), \quad (6)$$

where m_0 is the initial value of m before the step, m_∞ the equilibrium value of m at the new potential, and τ_m the time constant at which m makes its exponential approach toward m_∞.

Two special forms of Eq. 6 were used to model results in this paper. Activation kinetics were studied by holding the cell at −60 mV, where $m_0 = 0$. This simplifies the expression for m such that substitution into Eq. 1 results in the following equations for I_{Ba} activation:

$$i(t) = I_{ss}[1 - \exp(-t/\tau_m)]^a \quad (7)$$

where

$$I_{ss} = m_\infty^a g_{max}(V_m - E_r). \quad (8)$$

The time course of I_{Ba} activation was modeled with Eq. 7 by first selecting a value for a (e.g., 2 or 3) and then finding the τ_m (a nonlinear parameter) that provided the best fit using the MATLAB-supplied Nelder-Mead simplex algorithm. Steady-state current, I_{ss} (a linear parameter), was determined by least-squares minimization. Similar procedures were followed for fitting linear and nonlinear parameters to other equations used in this study (Boltzmann functions, exponentials, time shifts).

Deactivation kinetics were modeled at repolarizing potentials negative to −40 mV where $m_\infty = 0$. This simplifies the expression for m such that substitution into Eq. 1 results in the following equations for I_{Ba} deactivation:

$$i_{tail}(t) = I_{tail}\exp(-at/\tau_m) \quad (9)$$

and

$$I_{tail} = m_0^a g_{max}(V_m - E_r), \quad (10)$$

where I_{tail} is the magnitude of the tail current.

RESULTS

Chick cochlear hair cells only express L-type calcium current

Previous results have shown that chick cochlear hair cells possess a variety of K^+ currents (Fuchs and Evans, 1990) in addition to the Ca^{2+} current (Fuchs et al., 1990) described in detail in this paper. To isolate the relatively small Ca^{2+} current, we first loaded the patch pipettes with a high Cs^+ solution to block the much larger K^+ currents. The K^+ currents that remained were effectively blocked by perfusion with a 20 mM Ba^{2+} solution. Inward Ba^{2+} current through calcium channels will be referred to as I_{Ba}.

A previous study of chick cochlear hair cells found that nifedipine, a DHP antagonist, could block up to 40% of inward barium current (Fuchs et al., 1990) at a concentration of 10 μM. Since this DHP concentration blocks nearly all L-type calcium current in other cell types (e.g., ventricular myocytes (Balke et al., 1992), skeletal muscle (Sánchez and Stefani, 1978), photoreceptors (Barnes and Hille, 1989)), the possibility exists that hair cells express more than one type of calcium channel. So we performed a series of pharmacological experiments on a population of tall hair cells to attempt to dissect I_{Ba} into multiple components. Peptide toxins specific for N- (1–13 μM ω-conotoxin GVIA, $n = 5$), P- (100 nM ω-agatoxin IVa, $n = 7$), and Q-type (1 μM ω-conotoxin MVIIC, $n = 3$) calcium channels were ineffective in blocking I_{Ba} (data not shown). Thus, it appears that chick cochlear hair cells do not express a significant population of N-, P-, or Q-type calcium channels. So we reexamined the blocking effect of nifedipine and tested other DHP antagonists which might produce a more potent block.

In three cells, 10 μM nifedipine reduced I_{Ba} an average of 43%, comparable to the 26% block obtained by Fuchs et al. (1990). At 10 μM, the DHP antagonists nimodipine ($n = 3$) and nitrendipine ($n = 1$) were both more effective than nifedipine, reducing I_{Ba} by 72% and 50%, respectively. The effects of nimodipine are shown in greater detail in Fig. 1. Panel *A* (*left*) shows that 10 μM nimodipine reduced the steady-state current evoked by a −60 to 0 mV pulse by 73%. The residual current was then scaled up to the same level as the control trace which revealed that the kinetics of activation and deactivation of the residual current were nearly identical to those of the control current. Panel *B* shows that the residual I_{Ba} also had a voltage dependence of activation indistinguishable from control I_{Ba}. These results are consistent with the interpretation that hair cells express a single class of L-type calcium channels that are only partially blocked by 10 μM DHP antagonist.

Further support for this hypothesis comes from experiments using the DHP agonist Bay K 8644. If a significant fraction of the control current was DHP-insensitive, then one would expect a rapidly deactivating component to remain after Bay K 8644 treatment. Fig. 2 shows that Bay K 8644 (5 μM, $n = 2$) had typical DHP agonist effects on chick hair

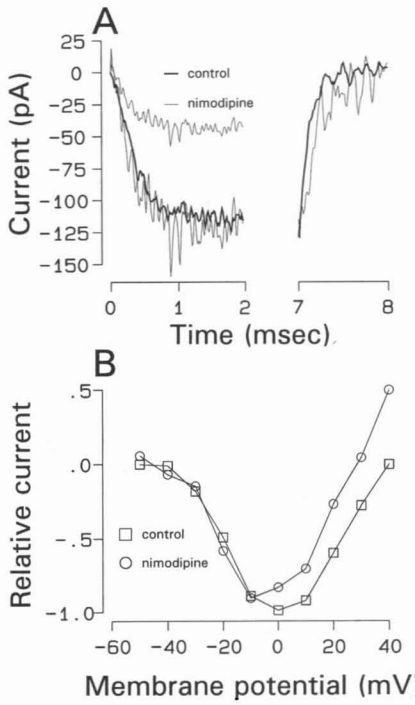

FIGURE 1 The kinetics and voltage dependence of activation of the residual current after blockade with 10 μM nimodipine was indistinguishable from control I_{Ba}. (*A, left*) Inward barium current was activated with a 7-ms voltage pulse from −60 to 0 mV. Only the first 2 ms is plotted to show that in the absence of drug I_{Ba} rapidly activated to a steady-state level of −116 pA (*thick line*). After bath exchange with 10 μM nimodipine, I_{Ba} decreased to −42 pA (*thin line*). This residual current was scaled by a factor of 2.8 so that its steady-state level was comparable to the control trace. (*A, right*) Tail currents upon repolarization to −60 mV are shown for control (*thick line*) and nimodipine (scaled by 2.8, *thin line*). Digitization interval: 14 μs. P/4 leak subtraction. Data from tall hair cell CSc31. R_s = 5 MΩ. C_m = 8.5 pF. (*B*) Normalized *I-V* curves of I_{Ba} with control TEA-Ba (*squares*) and 10 μM nimodipine (*circles*). Steady-state current was obtained by averaging current over the final 1.4 ms of the voltage step. Data from same cell as in *A*.

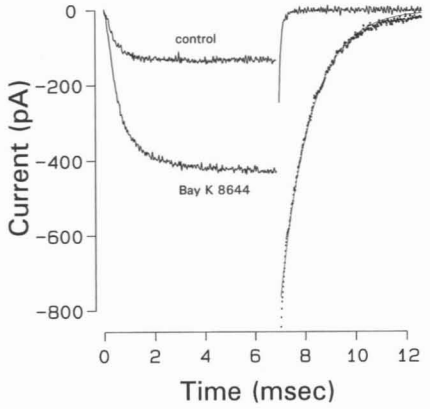

FIGURE 2 Effect of 5 μM Bay K 8644 on I_{Ba}. Inward current was activated with a 7-ms voltage pulse from −60 to 0 mV. I_{Ba} increased from −132 pA to −424 pA after bath exchange with a TEA-Ba solution containing 5 μM Bay K 8644. The tail current upon repolarization to −60 mV (at t = 7 ms) rapidly deactivated (τ_d = 0.1 ms) under control conditions. After exposure to Bay K 8644 the tail current (*solid points*) slowed dramatically and was well fit with a single exponential (*solid line*, τ_d = 1.23 ms). Digitization interval: 14 μs. P/4 leak subtraction. Data from tall hair cell CSc19. R_s = 3.2 MΩ. C_m = 6.9 pF.

cells, increasing barium current 4-fold and slowing the kinetics of deactivation nearly 10-fold. Note that the tail current under the influence of Bay K 8644 was extremely well fit by a single exponential with a time constant of 1.2 ms. The results of Figs. 1 and 2 combined with the inability of N-, P-, and Q-type calcium channel antagonists to block I_{Ba} strongly suggests that hair cells only express L-type calcium channels.

To test for the presence of an inactivating calcium or sodium current in chick hair cells, inward currents were evoked from a range of holding potentials. No differences were observed in the magnitude or time course of activation of inward current when holding potential was changed from −40 to −80 mV (Fig. 3 *A*). As expected, the inward current deactivated more slowly at −40 mV (see Fig. 11 for details on the voltage dependence of the deactivation time constant). The effect of holding potential was examined in greater detail by measuring steady-state *I-V* curves from holding potentials of −40, −60, and −80 mV (Fig. 3 *B*). No differences were observed in the magnitude of inward current over this range of holding potentials. Similar results were obtained in short hair cells.

The voltage dependence and kinetics of I_{Ba} were studied over the voltage range −50 to +60 mV, two examples of which are shown in Fig. 4. Inward current was first detectable at −40 mV, peaked at 0 mV (*top*), then declined toward 0 at positive membrane potentials (*bottom*). At negative potentials the inward current slowly increased, whereas at potentials positive to +20 mV the inward current decayed slightly. The time constant of the sag or decay of the inward current progressively decreased with further depolarization. The simplest interpretation of this effect is that it reflects the activation of incompletely blocked potassium channels which have a reversal potential in the 0 to +20 mV range under these particular ionic conditions. This reflects the fact that outward current can be carried by cesium ions through delayed rectifier and A-type potassium channels of chick cochlear hair cells (data not shown).

Inward tail currents upon repolarization to −60 mV are shown on an expanded time scale. The tail currents decayed exponentially with a time course that was best fit with two time constants, the fast component being ~170 μs, the slow one on the order of several milliseconds. A slow component of deactivation is consistent with a residual unblocked delayed rectifier or A-current.

H-H Model of I_{Ba}: Exponent of activation

Our kinetic analysis of I_{Ba} follows the model introduced by Hodgkin and Huxley in 1952 (which we call the H-H model) to describe sodium and potassium currents in squid giant axon. Fig. 5 illustrates the method by which the activation time constant, τ_m, and the exponent of activation, a, were determined. Equation 7 was fit to the activation of the barium current with both m^2 (a = 2) and m^3 (a = 3) kinetics to test which would provide the better fit. Visual inspection of the

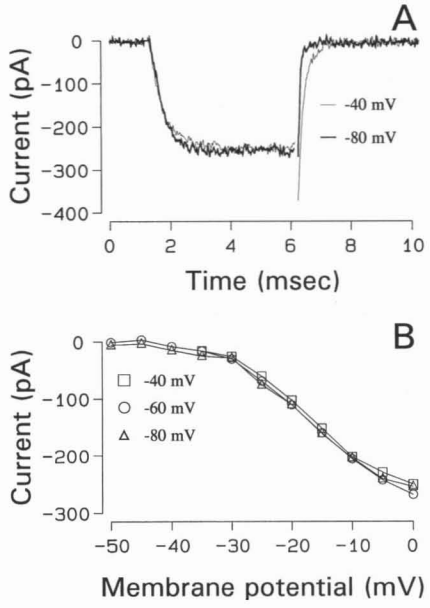

FIGURE 3 Effect of holding potential on I_{Ba}. (*A*) The cell was held at either −40 (*thin line*) or −80 mV (*thick line*), pulsed to 0 mV for 5 ms, then repolarized to the holding potential. The time courses of I_{Ba} activation were nearly identical at the two holding potentials. As expected, I_{Ba} deactivated much faster at −80 mV. Mean of 6 presentations. (*B*) Comparison of steady-state *I-V* curves evoked from holding potentials of −40 (□), −60 (○) and −80 mV (△) using 5-ms voltage pulse protocol as in *A*. Each point on the *I-V* curve is the steady-state current averaged over the final 2 ms of the response. Data from tall hair cell CSb01. R_s = 3.6 MΩ. C_m = 7.6 pF. Digitization rate: 100 kHz. P/4 leak subtraction.

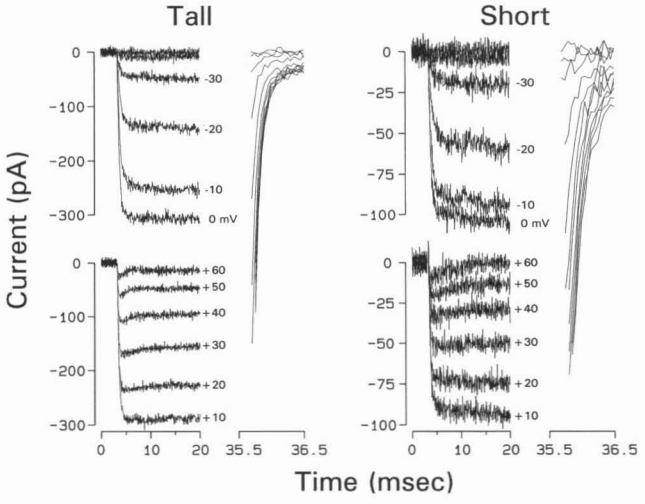

FIGURE 4 Whole cell currents were evoked from a holding potential of −60 mV to the potential indicated next to each trace (average of 6 presentations). The currents evoked over the voltage range +10 to +60 mV are shown below on a separate graph for clarity. Upon repolarization to −60 mV (35.7–36.5 ms), large inward tail currents were evident (all of which are plotted on the *top* scale). Note that the interval from 20–35.65 ms is suppressed and that the time base for the subsequent tail current is greatly expanded. (*Left*) Tall cell (CSb01). R_s = 3.6 MΩ. (*Right*) Short cell (CSa36). R_s = 8.9 MΩ. The two cells had similar kinetics and voltage dependence of activation despite the threefold difference in current magnitude (note that the ordinate scales are different). Cesium internal solution. Barium external solution. P/4 leak subtraction. Digitization rate: 20 kHz.

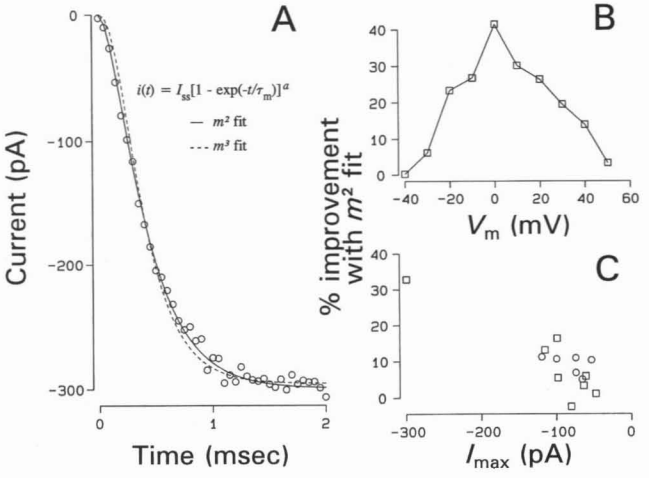

FIGURE 5 Determination of I_{Ba} activation time constant, τ_m. (*A*) The time course of Ba^{2+} current activation was fit to a standard Hodgkin-Huxley model with either m^2 (——, τ_m = 297 μs) or m^3 (- - - -, τ_m = 233 μs) kinetics. The H-H model parameters were fit to the data over a 2.5-ms interval beginning with the first point that came back to baseline (±2 s.d.) following the voltage pulse (defined as time 0 for the purposes of this fitting procedure). The current trace shown (○) was selected from the tall hair cell *I-V* curve of Fig. 4 (0 mV trace). (*B*) Mean squared errors were calculated for both m^2 and m^3 fits and the percent improvement in fit with m^2 kinetics computed for the cell of *A*. m^2 kinetics provided an improvement of 25–40% over m^3 kinetics in the −20 to +20 mV range where the inward current is largest. *Solid line* connects the points. (*C*) The comparison of m^2 versus m^3 kinetics illustrated in *B* was performed on 14 cells. The improvement in fit with m^2 kinetics was averaged over the −10, 0 and +10 mV records and plotted as a function of maximum steady-state current (I_{max}). *Squares* and *circles* are data points for tall and short hair cells, respectively.

theoretical fits (Fig. 5 *A*) suggests that m^2 kinetics are more appropriate. A quantitative comparison of m^2 versus m^3 kinetics is shown in Fig. 5, *B* and *C*. Each current trace of the *I-V* curve for this cell was fit with both m^2 and m^3 kinetics and the mean squared error computed for both fits. The error was 25–40% less with m^2 kinetics in the voltage range −20 to +20 mV, where the inward current was largest (Fig. 5 *B*). This comparison of m^2 versus m^3 kinetics was performed on a total of 14 cells and the results shown in Fig. 5 *C*. The percent reduction of mean squared error with m^2 kinetics was averaged over the −10 to +10 mV range (where I_{Ba} was largest) and plotted as a function of maximum steady-state current (I_{max}). There was a general trend indicating that cells with larger inward currents (and hence a better signal to noise ratio) showed a greater improvement in fit with m^2 kinetics. When the exponent of activation, *a*, was allowed to be a free nonlinear parameter in the curve fitting procedure, its mean value over the voltage range −20 to +20 mV was 1.73 (14 cells). We conclude that m^2 kinetics are an appropriate model for the time course of I_{Ba} activation.

Steady-state activation

Conductance-voltage (*G-V*) curves were derived from steady-state *I-V* curves by applying Ohm's Law (i.e., Eq. 8: $m_\infty^2 g_{max} = I_{ss}/[V_m - E_r]$). An empirical approach was taken

to determine E_r, the reversal potential of I_{Ba}, which is illustrated in Fig. 6 *A*. Above +20 mV the *I-V* curves were well approximated with a straight line. Thus, it appears that the conductance had already reached a maximal level (i.e., $m_\infty = 1$) by +20 mV and that the decay phase of the *I-V* curve was due solely to a linear decrease in driving force as V_m approached the reversal potential. A linear least-squares fit to the *I-V* curve over the +20 to +50 mV range was extrapolated to find E_r (*dashed line*), the mean value of which was +64 ± 5 mV (range: +57 to +75 mV, n = 14).

The assumption that g_{max} was constant over the entire activation voltage range was tested by measuring instantaneous *I-V* curves. This protocol also tested for voltage-dependent ion block, however unlikely for a calcium channel. The instantaneous *I-V* curve protocol repolarized the cell to a range of hyperpolarizing levels following a −60 to 0 mV prepulse. Since the prepulse to 0 mV always set m_∞ to a value near 1, tail currents in response to the repolarizing pulse extrapolated to time 0 should only reflect changes in driving force. A linear least squares fit (*dotted line*) to the instantaneous *I-V* curve (*squares*) over the −50 to −20 mV range extrapolated reasonably well to the decay phase of the *I-V* curve in the +20 to +50 mV range. The slope of least squared fits to instantaneous and standard *I-V* curves (which provide an estimate of g_{max}) agreed to within 21 ± 15% (range: 1 to 43%, n = 11). Thus, the assumption that g_{max} is constant over the activation voltage range of I_{Ba} appears valid. Values of E_r obtained from instantaneous *I-V* curves showed much greater variation (mean: +47 ± 17 mV, range: +23 to +77 mV) than those derived from the standard *I-V* curves due to the large amount of extrapolation required. Thus, the more consistent estimate of E_r derived from standard *I-V* curves (+64 mV) was used to compute the driving force for I_{Ba}.

The *G-V* curve (Fig. 6 *B*, *circles*) was computed by dividing I_{ss} (as derived by the fitting procedure of Fig. 5) by the driving force, then fit with a Boltzmann function (*solid line*):

$$g = \frac{g_{max}}{1 + \exp[(V_{1/2} - V_m)/\kappa]}, \quad (11)$$

where g_{max} is the maximal conductance, $V_{1/2}$ the half-activation voltage, and κ the steepness factor (g_{max} = 5.4 nS, $V_{1/2}$ = −13 mV and κ = 7.2 mV for this particular cell). The Boltzmann fits were normalized (dividing by g_{max}) and averaged (14 cells) to derive a mean steady-state activation curve, m_∞^2 (Fig. 7 *A*, *circles*). The Boltzmann parameters of Eq. 11 that gave the best fit to the mean activation curve were $V_{1/2}$ = −15 mV and κ = 7.8 mV (*solid line*).

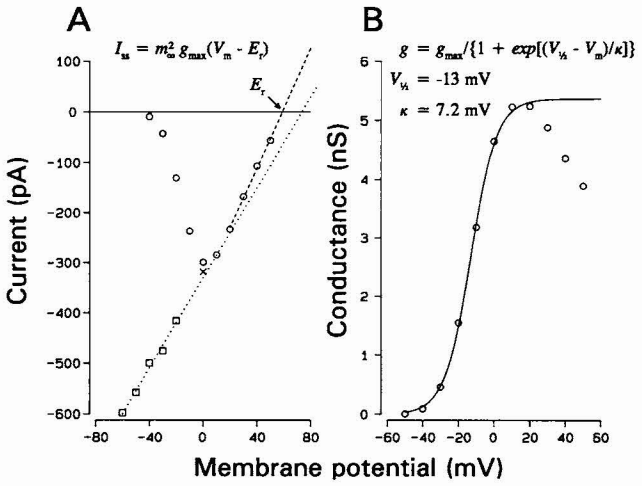

FIGURE 6 Determination of steady-state conductance-voltage (*G-V*) relation for a single cell. (*A*) The reversal potential, E_r, was calculated by extrapolating a linear least squares fit (- - - -) to the *I-V* curve (○) in the +20 to +50 mV range. Reversal potentials from 14 cells were averaged (E_r = +64 mV) to construct a standard driving force function, $V_m - E_r$. Also displayed on the graph is the instantaneous *I-V* curve determined after a −60 to 0 mV test pulse. Tail currents were measured after the test pulse by repolarizing the cell over the −20 to −110 mV range (only the −20 to −60 mV results are shown) and were fit with either a double exponential or a single exponential with a pedestal. The rapidly deactivating component of the tail current was extrapolated back to the time of repolarization (20 μs after the command pulse to the amplifier) and plotted as a function of repolarization level (□). The sustained current to the −60 to 0 mV test pulse (×) was of the same magnitude as the current recorded during the standard *I-V* curve protocol indicating that the inward current was stable. (*B*) *G-V* curve derived by dividing the steady-state inward current, I_{ss} (as derived by the fitting procedure of Fig. 5), by the driving force. The *G-V* curve was fit over the −50 to +20 mV range with a Boltzmann function (——). At more depolarized levels, the conductance values sagged from the saturating level (g_{max}) because of the smaller E_r for this cell (+59 mV) relative to the mean E_r (+64 mV). Data shown are for cell CSb01. R_s = 3.6 MΩ.

Opening and closing rate constants

Opening and closing rate constants were calculated from the steady-state activation parameter, m_∞, and time constant of

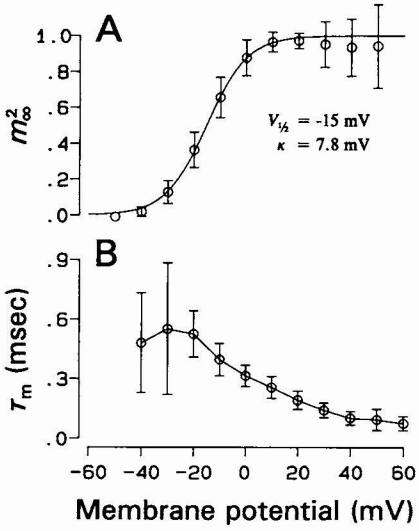

FIGURE 7 Voltage dependence of steady-state activation curve and time constant of activation. (*A*) A mean steady-state activation curve (○, ±1 s.d.) was obtained by normalizing and averaging (14 cells) the *G-V* curves obtained using the procedure of Fig. 6. *Solid line* is the Boltzmann fit to the averaged curve ($V_{1/2}$ = −15 mV, κ = 7.8 mV). (*B*) Voltage dependence of activation time constant derived with m^2 kinetics using fitting procedure of Fig. 5. Mean of 14 cells (○, ± 1 s.d.). *Solid line* connects the data points.

activation, τ_m, by rearranging Eqs. 4 and 5 to yield

$$\alpha_m = m_\infty/\tau_m \tag{12}$$

and

$$\beta_m = (1 - m_\infty)/\tau_m, \tag{13}$$

and are shown in Fig. 8 *A* and *B* (*circles*). The values of m_∞ and τ_m used to calculate the rate constants at any particular membrane potential (V_m) were the mean values shown in Fig. 7, *A* and *B*. Excellent fits to the rate constants were obtained with modified exponential functions similar to those used by others (Hodgkin and Huxley, 1952; Sánchez and Stefani, 1983):

$$\bar{\alpha}_m = \frac{\alpha_0(V_m - E_\alpha)}{1 - \exp[(E_\alpha - V_m)/V_\alpha]} \tag{14}$$

and

$$\bar{\beta}_m = \frac{\beta_0(E_\beta - V_m)}{1 - \exp[(V_m - E_\beta)/V_\beta]}. \tag{15}$$

The empirical functions for the rate constants were evaluated to reconstruct theoretical curves for steady-state activation, $\bar{m}_\infty$ (Fig. 8 *C*, *thick line*), and time constant of activation, $\bar{\tau}_m$ (Fig. 8 *D*, *solid line*), using Eqs. 4 and 5. The excellent match between the theoretical curves for $\bar{m}_\infty$ and $\bar{\tau}_m$, and the mean values derived from the data is a consequence of the excellent fit that the modified exponentials provide for the rate constant curves. In contrast, when simple exponential functions were used to fit the rate constants (such as those used by Hudspeth and Lewis, 1988a), an adequate fit of m_∞ and τ_m could not be obtained over the entire activation voltage range.

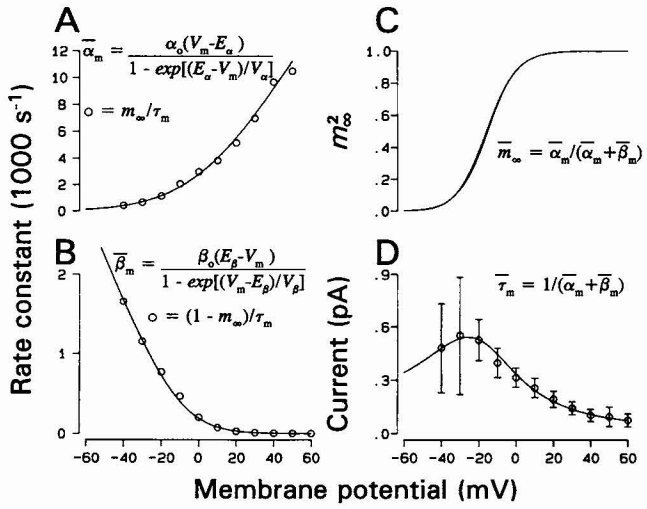

FIGURE 8 Theoretical fits of opening (α_m) and closing (β_m) rate constants and theoretical reconstruction of steady-state activation curve and time constant of activation. Opening (*A*, ○) and closing (*B*, ○) rate constants were calculated from the steady-state activation curve (m_∞^2; Fig. 7 *A*, ○) and time constant of activation (τ_m; Fig. 7 *B*, ○). The equations used to calculate α_m (Eq. 12) and β_m (Eq. 13) are indicated in their respective panels. The rate constants were fit with modified exponential functions (Eqs. 14 and 15) as indicated in the panels and plotted as *solid lines*. Best fits were obtained with the following values for the free parameters: E_α = 1.46 mV, V_α = 13.1 mV, α_0 = 226 $s^{-1}mV^{-1}$, E_β = −11.6 mV, V_β = 7.7 mV, β_0 = 58 $s^{-1}mV^{-1}$. (*C*) Comparison of the theoretical activation curve (*thick line* computed by evaluating the modified exponential function fits to rate constants as implied by equation shown in panel) and the Boltzmann function fit (*thin line*) to the mean steady-state activation curve (same curve as shown in Fig. 7 *A*). The two curves differ by no more than 3%. (*D*) Comparison of voltage dependence of theoretical $\bar{\tau}_m$ (*solid line*) and mean τ_m's derived by m^2 fits to data (*circles*, ± 1 s.d.; same data points as in Fig. 7 *B*).

Model *I-V* curves and waveforms of I_{Ba} activation

Model waveforms of I_{Ba} activation were constructed by combining Eqs. 7 and 8 (with m^2 kinetics) to yield:

$$i(t) = \bar{m}_\infty^2 \bar{g}_{max}(V_m - E_r)[1 - \exp(-t/\bar{\tau}_m)]^2, \tag{16}$$

where $\bar{m}_\infty$ and $\bar{\tau}_m$ were constructed from the modified exponential fits to the rate constant curves (fitted curves of Fig. 8 *C*, *D*), E_r = +64 mV, and $\bar{g}_{max}$ (the only cell-specific parameter) was determined by the procedure illustrated in Fig. 9. Multiplication of the activation curve, $\bar{m}_\infty^2$, by the driving force function, $V_m - E_r$, determined the shape of a model steady-state *I-V* curve. The model *I-V* curve was then scaled by the factor, $\bar{g}_{max}$, that minimized the least squared error between the theoretical (*solid line*) and the measured steady-state *I-V* curve, I_{ss} (*circles*). Evaluation of Eq. 16 with cell-specific $\bar{g}_{max}$ values provides an excellent fit to the time course of I_{Ba} activation over the −40 to +40 mV range (Fig. 10) for both tall (*left*) and short (*right*) hair cells.

Analysis of I_{Ba} tail currents

The construction of the H-H model for I_{Ba} has been based solely on the activation properties of I_{Ba}. An excellent test of

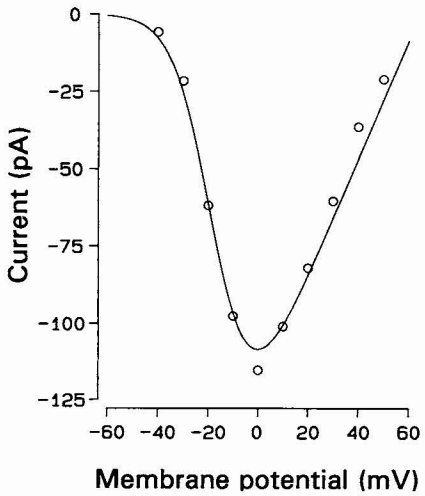

FIGURE 9 Theoretical fits (——) to individual steady-state *I-V* curves were constructed by finding the scaling factor, $\bar{g}_{max}$, that minimized the mean squared error between I_{ss} (○) and a scaled version of the model *I-V* curve: $\bar{g}_{max}\bar{m}_\infty^2(V_m - E_r)$. *I-V* curve shown is for tall cell CSa32 ($\bar{g}_{max}$ = 1.9 nS, R_s = 5.8 MΩ).

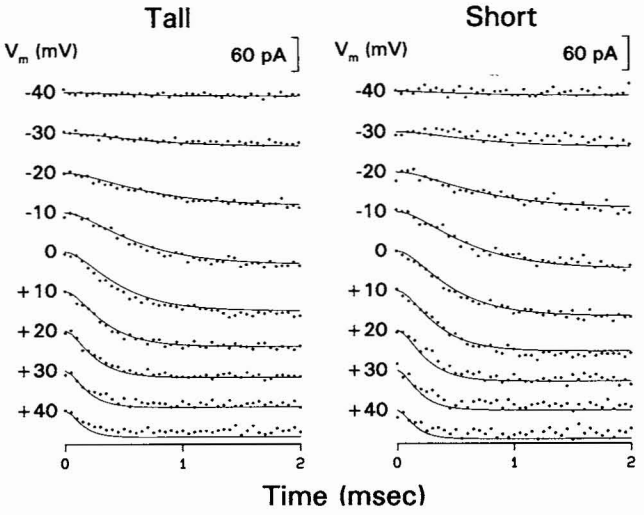

FIGURE 10 Model waveforms of I_{Ba} activation (——) were constructed according to Eq. 16 for a tall (CSa32, *left*; R_s = 5.8 MΩ) and a short (CSa34, *right*; R_s = 6.7 MΩ) hair cell and are compared to raw data (○) over the −40 to +40 mV range. Limiting conductance, $\bar{g}_{max}$ (the only cell-dependent parameter), was computed for each cell according to the procedure described in Fig. 9. Time 0 corresponds to 150 μs following the voltage step from the −60 mV holding potential.

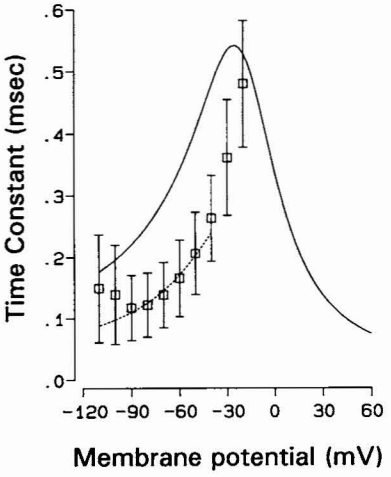

FIGURE 11 Comparison of H-H model prediction to measured deactivation time constants. Theoretical curve of $\bar{\tau}_m$ (——) calculated from modified exponential function fits to rate constants (i.e., same curve as Fig. 8 *D*) evaluated over the range −110 to +60 mV. (□) Time constants of deactivation, τ_d, derived from instantaneous *I-V* curves (mean of 14 cells ± 1 s.d.). Tail currents following a test pulse from −60 to 0 mV were fit with either a double exponential or a single exponential with a pedestal and the fast time constant plotted as a function of repolarization potential. (- - - -) Predicted values of τ_d from H-H model, i.e., $\bar{\tau}_m/2$. Note the excellent agreement between τ_d and the model prediction over the −90 to −40 mV range. The slower than expected values of τ_d at repolarization potentials of −100 and −110 mV are probably due to an inability of the voltage clamp to rapidly charge the membrane following such large voltage steps. At potentials more depolarized than −40 mV, I_{Ba} does not completely deactivate and the relation, $\tau_d = \bar{\tau}_m/2$, is no longer valid.

the model would be to compare its predictions to measurements of I_{Ba} tail currents. Time constants of deactivation, τ_d, were measured from instantaneous *I-V* curves (as introduced in Fig. 6) over the range −110 to −20 mV. m^2 kinetics dictate that τ_d should be twice as fast as τ_m (see Eq. 9). Fig. 11 shows the results of this test. There was excellent agreement between τ_d (*squares*) and the model prediction (*dashed line*) over the −90 to −40 mV range. This result supports the conclusion that m^2 kinetics are an appropriate model for I_{Ba} activation.

In Fig. 12 we compare predicted magnitudes of tail currents to those measured from the raw data. Tail currents were recorded using the standard *I-V* curve protocol described in Fig. 4 (−60 mV holding/repolarization potential) and were fit with a double exponential or a single exponential with a pedestal. The magnitude of the tail current, I_{tail}, was determined by extrapolating the fast exponential to a time, t_d, following repolarization corresponding to a membrane potential of −54 mV (to correct for charging time, see Appendix for details). I_{tail}-*V* curves computed in such a manner are shown for a representative tall (*circles*) and short (*triangles*) hair cell. Equation 10, $I_{tail} = \bar{m}_0^2 \bar{g}_{max}(V_{rep} - E_r)$, was used to compute model I_{tail}-*V* curves using cell-specific $\bar{g}_{max}$ values as described in Fig. 9. Both cases show excellent agreement over the entire voltage range, indicating that the method we use to extrapolate tail currents is valid. This result also provides additional evidence that the instantaneous channel conductance is voltage-independent and that the assumed reversal potential of I_{Ba} is reasonable.

The final comparison of the H-H model to our data is shown in Fig. 13 where the time course of deactivation of the tail current is compared with the model prediction (shifted by voltage-dependent t_d values). For both the tall and short hair cell, there is excellent agreement with the H-H model over the entire −40 to +40 mV range.

DISCUSSION

Chick cochlear hair cells only express L-type calcium channels

The results presented here represent the most detailed pharmacological and kinetic study of a hair cell Ca^{2+} current to date. Several lines of evidence support our conclusion that chick hair cells predominantly, if not exclusively, express L-type calcium channels: 1) The DHP antagonist nimodipine blocked 73% of I_{Ba} at a concentration of 10 μM. Since this concentration blocks nearly all L-type current in other preparations, we examined the kinetics of the residual current after nimodipine block. The voltage dependence of activation as well as the time course of activation and deactivation of the residual current were nearly identical to that of control I_{Ba}. Our interpretation of this result is that 10 μM is a submaximal blocking level of DHP antagonist on chick hair cell calcium channels which results in a residual current that is indistinguishable from control I_{Ba}. 2) Bay K 8644 had typical DHP agonist effects, increasing the steady-state I_{Ba} nearly threefold and slowing the tail current 10-fold. The fact that the tail current was well fit by a single exponential argues that a

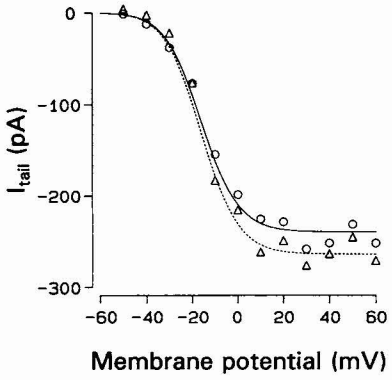

FIGURE 12 Comparison of H-H model prediction of I_{Ba} tail current magnitude to those measured by extrapolating tail currents to a voltage-dependent time after repolarization corresponding to a membrane potential of −54 mV (see Appendix for details). Model predictions were computed by evaluating Eq. 10: $I_{tail} = \bar{m}_0^2 \bar{g}_{max}(V_{rep} - E_r)$, where $V_{rep} = -60$ mV, $E_r = +64$ mV, $\bar{g}_{max}$ derived according to procedure of Fig. 9 for each cell, and $\bar{m}_0^2$ is the theoretical curve for steady-state activation (from Fig. 8 *C*). Note the excellent agreement between respective theoretical and experimental values for a representative tall (——, ○: CSa32; $R_s = 5.8$ MΩ) and short (- - - -, △: CSa34; $R_s = 6.7$ MΩ) hair cell.

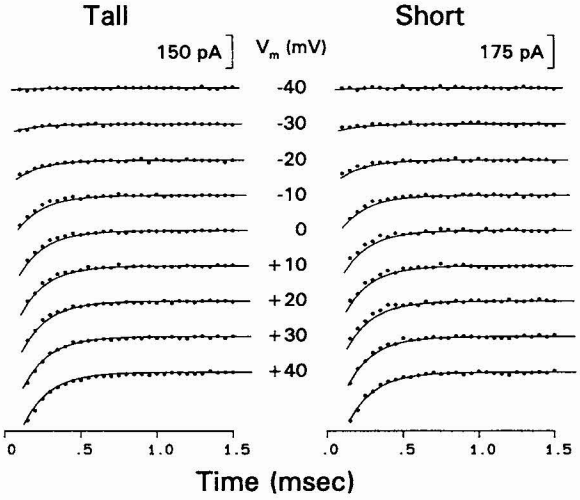

FIGURE 13 H-H model of the magnitude and time course of I_{Ba} deactivation compared with measured I_{Ba} tail currents. Tail currents were recorded using same *I-V* curve protocol described in Fig. 4. Time 0 corresponds to the time that the repolarization step to −60 mV is delivered to the patch amplifier. Tail currents were fit with either a double exponential or a single exponential with a pedestal. The slower exponential or pedestal value was subtracted from the raw tail currents before plotting. The artifact associated with the leak-subtracted capacitive transient during the first 100–150 μs of the tail current is suppressed. The H-H model predictions of I_{Ba} deactivation (——) are right-shifted by an amount corresponding to a repolarization potential of −54 mV (see Appendix). Note the excellent agreement between theoretical and experimental curves for a representative tall (*left*, CSa32; $R_s = 5.8$ MΩ) and short (*right*, CSa34; $R_s = 6.7$ MΩ) hair cell.

DHP-insensitive component was not present. 3) The peptide toxins ω-conotoxin GVIA, ω-agatoxin IVa, and ω-conotoxin MVIIC did not reduce I_{Ba}, thus eliminating N-, P-, and Q-type calcium channels as contributors to I_{Ba}. 4) Holding potentials as negative as −90 mV failed to reveal any inactivating Ba^{2+} currents which makes it unlikely that T-type Ca^{2+} channels are present in chick hair cells. 5) Kinetic analysis of I_{Ba} did not reveal multiple components. A kinetic model based on a single set of H-H parameters and derived solely from activation of Ba^{2+} current predicted very well the magnitude and time course of tail current deactivation. Activation curves were well fit by a single Boltzmann function and the time course of deactivation was well fit by a single exponential.

In summary, neither a pharmacological nor a kinetic approach revealed multiple classes of calcium channels in chick hair cells. While we cannot definitively rule out the presence of a minor DHP-insensitive component of I_{Ba}, if one is present then it has kinetic properties very much like the predominant DHP-sensitive component. Although the pharmacological experiments were only performed on tall hair cells, the fact that the H-H model provides an excellent fit to the Ba^{2+} current found in both tall and short hair cells suggests that short hair cells express the same class of calcium channels as tall hair cells. These may be previously unidentified members of the L-type class of voltage-gated calcium channels, as suggested by their rapid kinetics and relative insensitivity to DHP antagonists.

Steady-state activation

In Table 1 we compare the steady-state activation parameters of the chick hair cell Ca^{2+} current with putative L-type Ca^{2+} currents that have been characterized in a variety of other tissues. While L-type channels were originally described as high voltage-activated in dorsal root ganglion neurons (Nowycky et al., 1985; Fox et al., 1987), this does not appear to be a general property of DHP-sensitive Ca^{2+} channels. Half-activation voltages of L-type currents cover a >50 mV range from −39 mV (Roberts et al., 1990) to +12 mV (Taylor, 1988).

Screening of surface charges has generally been invoked as the most likely explanation for depolarizing shifts in activation curves as divalent cation strength is increased. By the same token, decreasing amounts of surface charge (which result in a greater potential gradient across the voltage-sensitive elements of the channel) would also be expected to produce depolarizing shifts in the activation curve. A major source of surface charge, at least for sodium channels, may come from sialic acid residues attached to glycosylation sites. However, the α_1 subunit of L-type Ca^{2+} channels does not appear to be heavily glycosylated (Leung et al., 1987; Takahashi et al., 1987; Tanabe et al., 1987; Mikami et al., 1989). Other variations such as charged amino acids in the primary sequence or interaction with other subunits could very easily explain the wide range of steady-state activation among L-type channels.

If we allow for a 5 mV hyperpolarizing shift in our activation curve by switching charge carriers from 20 mM Ba^{2+} to 4 mM Ca^{2+} (Zidanic, M., unpublished observations), then the half activation voltage of the chick cochlear hair cell Ca^{2+} current is within 5 mV of that characterized in turtle cochlea

TABLE 1 Comparison of steady-state activation parameters for putative L-type calcium channels

Reference	Tissue	$V_{1/2}$	κ	Charge carrier	Internal solution	Junction potential	Inactivating
		mV	mV	mM	mM	mV	
Zidanic and Fuchs (1995)*	Chick cochlea	−18	7.8	20 Ba^{2+}	130 CsCl	−3	No
Art et al. (1993)	Turtle cochlea	−26	8.6	2.8 Ca^{2+}	125 CsCl	−4	No
Roberts et al. (1990)‡	Frog sacculus	−39	5.1	4 Ca^{2+}	106 CsAsp	−13	No
Bader et al. (1982)	Salamander rods	−18	6.0	3 Ca^{2+}	Single-microelectrode clamp		No
Taylor (1988)§	Cat d.r.g.	+12	8.3	10 Ca^{2+}	140 CsCl	‖	No
Fox et al. (1987)	Chick d.r.g.	+2	4.0	10 Ca^{2+}	100 CsCl	‖	Yes
Artalejo et al. (1991)¶	Bovine chromaffin	−10		10 Ba^{2+}	100 CsCl	‖	Yes
Sánchez and Stefani (1983)**	Frog sartorius	−21	7.6	10 Ca^{2+}	Three-microelectrode clamp		Yes
Markwardt and Nilius (1988)	Guinea pig ventricle	−28	3.7	5 Ba^{2+}	140 Tris-Cl	‖	Yes
Bean (1985)‡‡	Canine atrium	−5		5 Ca^{2+}	120 CsCl	‖	Yes

*$V_{1/2}$ has been shifted by −3 mV to correct for the junction potential.

‡The $V_{1/2}$ and κ values tabulated here are the mean of four cells. A junction potential correction of −13 mV was used (the value of −3 mV in Table 1 of Roberts et al. (1990) is a typographical error) (W.M. Roberts, personal communication).

§This author used a modified Boltzmann function of the form $1/\{1 + E_2 + E_1E_2\}$, where $E_i = \exp[(V_i - V_m)/K_i]$, to model activation curves. In order to make these results directly comparable, we evaluated the modified Boltzmann function over a suitable voltage range, then fit the curve with a Boltzmann function of the form $1/\{1 + \exp[(V_{1/2} - V_m)/\kappa]\}$. The values of $V_{1/2}$ and κ that provided the best fit are tabulated.

‖No mention is made of junction potential correction by these authors.

¶$V_{1/2}$ was determined by eye from their "facilitation" current *I-V* plot of Fig. 5 *B*. Steepness factors were not reported.

**These authors used a "cubic" Boltzmann function of the form $1/\{1 + \exp[(V_{1/2} - V_m)/k]\}^3$ to model activation curves. To make their results directly comparable, we evaluated their cubic Boltzmann functions over a suitable voltage range, then fit the curve with a Boltzmann function of the form $1/\{1 + \exp[(V_{1/2} - V_m)/\kappa]\}$. The values of $V_{1/2}$ and κ that provided the best fit are tabulated.

‡‡$V_{1/2}$ was determined by eye from the "I_{slow}" *I-V* curve of Fig. 5. Steepness factors were not reported.

(Art et al., 1993), salamander photoreceptors (Bader et al., 1982; Corey et al., 1984; Barnes and Hille, 1989), frog skeletal muscle (Sánchez and Stefani, 1983), bovine (Reuter and Scholz, 1977) and guinea pig ventricle (Markwardt and Nilius, 1988; Rose et al., 1992). Recent data from the frog sacculus (Roberts et al., 1990) and crista ampullaris (Prigioni et al., 1992) indicate that Ca^{2+} currents in these hair cells may activate at potentials nearly 15 mV more hyperpolarized than those from the chick or turtle cochlea. In contrast, L-type Ca^{2+} channels have been described in chick (Fox et al., 1987) and cat (Taylor, 1988) dorsal root ganglion neurons, bovine chromaffin cells (Fenwick et al., 1982; Artalejo et al., 1991) and canine atrium (Bean, 1985) that appear to activate at potentials 15–20 mV more depolarized than other L-type Ca^{2+} channels.

Kinetics of I_{Ca}

Two independent methods verified that an appropriate exponent of activation was used in the H-H model. First, an error analysis showed that m^2 kinetics gave a better fit to the time course of I_{Ba} activation than did m^3 kinetics. Second, the deactivation time constants measured with an instantaneous *I-V* curve protocol matched very well those predicted by the H-H model (derived with m^2 kinetics). Ohmori (1984) reached a similar conclusion based on measured time constants of activation and deactivation using a 100 mM Ba^{2+} solution at 9°C. Art and Fettiplace (1987) also used m^2 kinetics to describe the activation of I_{Ca} in turtle cochlear hair cells, whereas Hudspeth and Lewis (1988a) used m^3 kinetics for activation of I_{Ca} in bullfrog saccular hair cells. Whether the exponents of activation used in the turtle and frog hair cell preparations would survive the tests of error analysis or comparison with deactivation time constants remains an open question.

The activation time constants of I_{Ba} (0.3–0.6 ms) described here are consistent with those described previously for chick hair cells (Fuchs et al., 1990) as well as with the kinetics of I_{Ca} described in turtle (Art and Fettiplace, 1987) and frog hair cells (Hudspeth and Lewis, 1988a; Roberts et al., 1990). However, the time constants of activation (τ_m) reported here are nearly twice as fast as those reported in a previous study of chick hair cells (Fig. 7; Ohmori, 1984) which were made under ionic conditions similar to ours and at nearly the same temperature. One methodological difference is that Ohmori used patch pipettes with initial resistances from 5–10 MΩ, whereas we used pipettes with resistances no greater than 3.5 MΩ and achieved voltage clamp time constants as fast as 28 μs. The slower clamp speeds expected from higher resistance pipettes would be expected to result in the measurement of slower τ_m's.

Hair cell Ca^{2+} currents differ from other L-type channels by virtue of their rapid kinetics. For example, L-type channels in photoreceptors (Fig. 5; Corey et al., 1984), cat dorsal root ganglion neurons (Fig. 7; Taylor, 1988), and guinea pig ventricle (Fig. 3; Markwardt and Nilius, 1988) activate with time constants in the 1–10 ms range. The slowest L-type channels appear to be localized to skeletal muscle where τ_m is 180 ms at the midpoint of the activation curve (Sánchez and Stefani, 1983). In terms of their noninactivation, half activation voltage, and time course of activation, hair cell Ca^{2+} currents more closely resemble P-type Ca^{2+} currents in cerebellar Purkinje cells (Regan, 1991) and presynaptic terminals of the squid stellate ganglion (Llinás et al., 1981; Augustine et al., 1985; Charlton and Augustine, 1990; Mintz et al., 1992).

Functional role of I_{Ca}

A growing body of evidence suggests that Ca^{2+} and Ca^{2+}-activated K^+ channels are colocalized, perhaps exclusively,

near neurotransmitter release sites (Roberts et al., 1990; Robitaille et al., 1993). Given the much higher density of afferent innervation to tall hair cells of the chick cochlea, such a scheme would predict larger Ca^{2+} currents in tall versus short hair cells. The limited population of cells characterized in this study precludes any quantitative comparison of Ca^{2+} current magnitudes, although it is worth noting that the largest Ca^{2+} current was recorded from a tall hair cell. Ongoing experiments in this laboratory support the hypothesis that tall hair cells have larger Ca^{2+} currents than do short hair cells (Fuchs and Fagan, 1993).

L-type Ca^{2+} channels are well known for their propensity to run down during whole-cell recordings and those found in hair cells are no exception (Ohmori, 1984). This phenomenon likely is linked to the loss of cytoplasmic factors that control the phosphorylation state of the Ca^{2+} channel (Yue et al., 1990; Mundiña-Weilenmann et al., 1991; Ma et al., 1992; Ono and Fozzard, 1992). Since the majority of hair cells in the avian cochlea receive both afferent and efferent innervation (Takasaka and Smith, 1971; Tanaka and Smith, 1978; Hirokawa, 1978; Fischer, 1992), it is not unreasonable to speculate that cochlear efferent neurotransmitters or neuromodulators exert some control over voltage-gated Ca^{2+} channels. Such a role may complement the inhibitory actions of acetylcholine that have been proposed to occur through the initial activation of a ligand-gated cation channel (Fuchs and Murrow, 1992a, b).

Potassium channels have recently been cloned from a chick cochlea cDNA library (Navaratnam and Oberholtzer, 1994) and the cloning of calcium channels will inevitably follow. The H-H model developed here should be useful to compare to the physiological properties of cloned calcium channels expressed in frog oocytes or transfected cells. In addition, this model can be used as a basis to describe how the characteristics of the Ca^{2+} current change as recording conditions approach the in vivo situation. One would predict that physiological external Ca^{2+} concentrations would produce a hyperpolarizing shift of the activation threshold whereas increasing temperature to the avian body temperature of 40°C could speed up the channel kinetics by at least a factor of two. Both of these factors would act in concert to increase the intrinsic frequency response of the hair cell membrane and may contribute to relatively high-frequency electrical tuning in the avian cochlea.

We are grateful to Drs. J. Karpen, S. R. Levinson, A. R. Martin, and two anonymous reviewers for providing helpful comments on the manuscript. We thank L. Stahl for technical assistance.

This work was supported by NIDCD grant DC00276 to P.A.F., training grant 2-T32-NS07083–11A1, and individual NRSA grant 1-F32-DC00086 to M.Z.

APPENDIX

Isopotential determination of tail current magnitude

This appendix describes the technique we have developed for computing tail current magnitudes. It differs from the usual method of using a fixed time after repolarization, t_d, that an exponential fit is extrapolated to determine the tail current magnitude. We first illustrate that the isochronal method is inadequate for measuring the I_{Ba} tail currents we have described in this paper. Fig. 14 shows tail currents calculated using two fixed values of t_d. With a value of t_d = 125 μs (*circles*), reasonable agreement is obtained in the saturating portion of the curve (+30 to +60 mV), but the tail currents are consistently underestimated (relative to their predicted value) in the activation phase of the curve (−20 to +20 mV). On the other hand, if the tail currents are extrapolated closer to the time of repolarization (i.e., t_d = 75 μs), agreement is obtained over the activation phase (−50 to 0 mV), but the tail currents are consistently larger in the saturation range (+10 to +60 mV). Given the rapid deactivation kinetics of I_{Ba} at the −60 mV repolarization potential (τ_d = 166 μs), it is not surprising that such small differences in the amount of extrapolation lead to large changes in the magnitude of I_{tail}. It is also clear that a single value for t_d to compute the I_{tail}-V curve cannot lead to agreement between the predicted and measured values for I_{tail}.

The most likely source of this discrepancy is the violation of the assumption that I_{tail} is always measured at a constant voltage, −60 mV. For slowly deactivating tail currents, a sufficiently large t_d can be picked with the isochronal method so that capacitive transients have decayed to near 0 and yet very little of the tail current has decayed. Thus, all tail currents can be measured at a potential very close to the desired repolarization potential. However, if the tail current decays rapidly as is the case with I_{Ba}, then very short extrapolation times must be used. With these very short extrapolation times, the capacitive transient may not have fully decayed and so the tail current may really be measured at a potential that is significantly positive to the repolarization potential. Fig. 15 illustrates this point. Capacitive transients were recorded in response to hyperpolarizing voltage pulses and the results from 6 cells shown in *A*. The capacitive currents were integrated, normalized, and plotted as a function of time (*B*). The curves in *B* describe the time course of membrane repolarization following a step change in voltage, which we represent with the function, $q(t)$. It is apparent that if a fixed t_d is used to extrapolate tail currents, then the actual voltage to which to the membrane is repolarized at time t_d varies with the magnitude of the voltage pulse. For example, if t_d = 75 μs is used for either of the two cells with the fast transients (where q(75 μs) = 0.8), a depolarization to −50 mV (ΔV = 10 mV) will reach −58 mV 75 μs after repolarization, whereas a depolarization to 0 mV (ΔV = 60 mV) will only reach −48 mV 75 μs after repolarization.

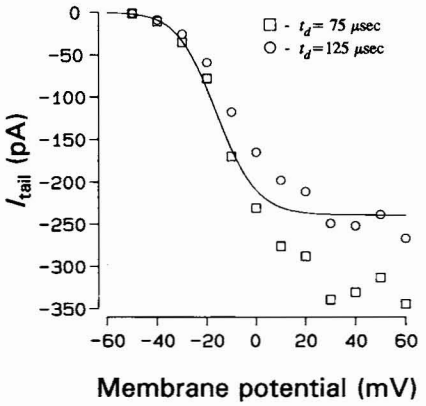

FIGURE 14 Comparison of I_{Ba} tail currents to H-H model prediction. Same *I-V* curve protocol as in Fig. 4. Tail current magnitudes were computed from the H-H model (——) according to Eq. 10: $I_{tail} = \bar{m}_0^2 \bar{g}_{max}(V_m - E_r)$, where $\bar{m}_0^2$ is derived from the theoretical fits to the rate constants (Fig. 8 *C*), E_r = +64 mV, V_m = −60 mV and $\bar{g}_{max}$ = 1.9 nS for the cell shown (tall cell CSa32, R_s = 5.8 MΩ). Tail currents were fit with a double exponential (or a single exponential with a pedestal) and the fast component extrapolated to either 75 (□) or 125 μs (○) following the repolarization pulse. The exponential fit of the tail current was performed over a 15 ms interval that began with the first valid data point following the artifact associated with the leak-subtracted capacitive transient (100–150 μs following the repolarization pulse to the amplifier for this particular cell).

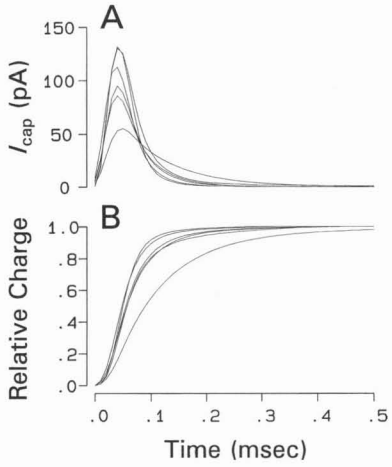

FIGURE 15 Capacitive transients and relative charge transfer in 6 selected cells. (*A*) Capacitive currents were measured by scaling and averaging the transients evoked from a holding potential of −60 mV to hyperpolarizing levels ranging from −65 to −80 mV (5 mV increments). Both the hyperpolarizing and repolarizing transients were averaged (3 repetitions) to minimize noise. The capacitive transients shown were normalized for a 1 mV voltage step. Time constants of an exponential fit to the decay phase of the transients, τ_{clamp} (clamp speed), ranged from 27.5 to 90 μs for the 6 cells shown. Digitization rate: 10 μs. (*B*) The capacitive transients were integrated (over the interval $10\tau_{clamp}$) and divided by the voltage step, ΔV, to calculate total membrane capacitance, C_m. Charge transfer was normalized to C_m and plotted as a function of time. Such a plot reflects the time course of membrane repolarization following a voltage pulse.

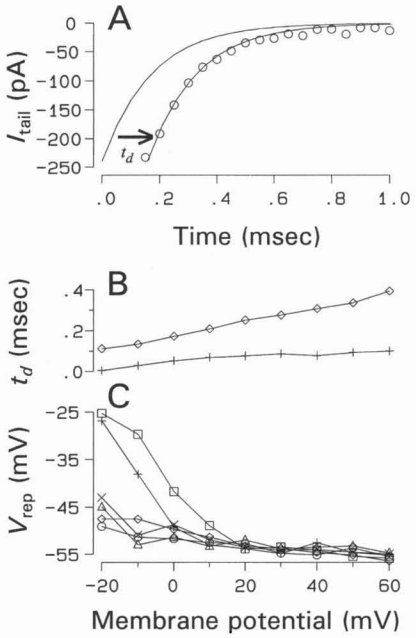

FIGURE 16 Method used to find optimal membrane potential at which tail currents should be measured to bring them into agreement with the H-H model. (*A*) Tail currents were first fit to either a double exponential or a single exponential with a pedestal. Then, the H-H model prediction for the tail current (——) was shifted by an amount, t_d = 160 μs, that provided the best fit of the model to the exponential representing the fast component of deactivation. Tail current shown was measured at −60 mV (○) following a −60 to +60 mV activating pulse (tall hair cell CSa32). The slow component of deactivation was first subtracted before plotting. (*B*) The shifting procedure in the *top panel* was performed for each trace of the *I-V* curve and the t_d values that provided best fits are plotted versus V_m for the two cells with the fastest (+, CSb01) and slowest clamp speeds (◇, CSb09) included in this analysis. (*C*) The t_d values obtained from the 6 cells were converted to a membrane potential, V_{rep}, according to: $V_{rep} = V_m - q(t_d)\,(V_m + 60)$, where $q(t)$ is the appropriate charge transfer curve of Fig. 15 *B*. + and ◇ represent the corresponding V_{rep} values for the cells whose t_d values are shown in *B*. Note how the t_d values consistently convert to a repolarization voltage of −52 to −56 mV in the saturating phase of the *I-V* curves (+20 to +60 mV) for all 6 cells despite the 4-fold range of t_d values.

The method described below uses an alternative approach to determine the I_{tail}-V curve and to resolve the apparent conflict between predicted and measured I_{Ba} tail currents. The extrapolation time was allowed to vary with the size of the voltage step such that the membrane potential was repolarized to a fixed voltage near −60 mV. To determine what might be the best repolarization voltage, a first pass was made through the data to find the values of t_d that made the extrapolated tail currents fit the prediction of the H-H model at each voltage level (Fig. 16 *A*). This procedure was performed for each tail current over the entire *I-V* curve and the results for two cells are shown in Fig. 16 *B*. Each t_d was then converted to a membrane potential, V_{rep}, which depends on the size of the repolarizing pulse and the time course of charge transfer, $q(t)$, for the cell under study. When V_{rep} is plotted as a function of depolarization level (Fig. 16 *C*), the mean value of V_{rep} for 6 cells with stable values in the +20 to +60 mV range is −54 mV.

Using V_{rep} = −54 mV, t_d was then computed as a function of V_m (Fig. 17) based on the time course of the charging transient. The cell with the fastest capacitive transient had t_d values that ranged from 18 μs at −50 mV to 91 μs at +60 mV. These voltage-dependent t_d values were used to calculate the tail current magnitudes that compared well with the predicted values in Fig. 12.

The preceding exercise illustrates very well the difficulty in accurately measuring tail current amplitudes when dealing with a channel with very rapid kinetics. In fact, had the H-H model based on the activation kinetics of I_{Ba} not been developed, a first pass could not have been made through the tail current data to determine the most appropriate V_{rep}. The general conclusion we may draw from this analysis is that if the speed of the voltage clamp is less than six times faster than the tail current time constant, then tail current amplitudes extrapolated to the same point in time may not yield accurate steady-state activation curves. In cases where there is some doubt as to the effects of clamp speed on extrapolated tail currents, it is highly recommended that steady-state *I-V* curves be obtained as well in order to verify the integrity of the activation curves.

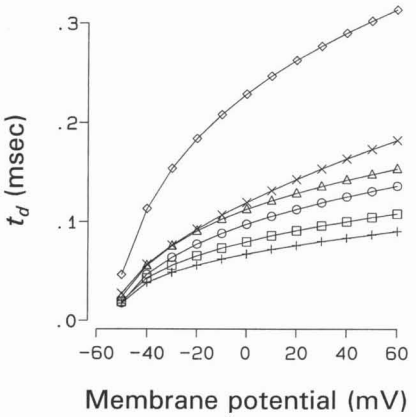

FIGURE 17 Voltage-dependent extrapolation times that correspond to a V_{rep} = −54 mV for 6 cells plotted as a function of depolarization level, V_m. Extrapolation times, t_d, were computed according to: $t_d = q^{-1}((V_m + 54)/(V_m + 60))$, where q^{-1} is the inverse function of q. The same symbol is used in both this figure and Fig. 16 to represent data from a given cell. *Solid lines* connect the symbols.

REFERENCES

Art, J. J., and R. Fettiplace. 1987. Variation of membrane properties in hair cells isolated from the turtle cochlea. *J. Physiol.* 385:207–242.

Art, J. J., R. Fettiplace., and Y.-C. Wu. 1993. The effects of low calcium on the voltage-dependent conductances involved in tuning of turtle hair cells. *J. Physiol.* 470:109–126.

Artajelo, C. R., M. K. Dahmer, R. L. Perlman, and A. P. Fox. 1991. Two types of Ca^{2+} currents are found in bovine chromaffin cells: facilitation is due to the recruitment of one type. *J. Physiol.* 432:681–707.

Ashmore, J. F. 1983. Frequency tuning in a frog vestibular organ. *Nature.* 304:536–538.

Ashmore, J. F., and D. Attwell. 1985. Models for electrical tuning in hair cells. *Proc. R. Soc. Lond. B.* 226:325–344.

Augustine, G. J., M. P. Charlton, and S. J. Smith. 1985. Calcium entry into voltage-clamped presynaptic terminals of squid. *J. Physiol.* 367: 143–162.

Bader, C. R., D. Bertrand, and E. A. Schwartz. 1982. Voltage-activated and calcium-activated currents studied in solitary rod inner segments from the salamander retina. *J. Physiol.* 331:253–284.

Balke, C. W., W. C. Rose, E. Marban, and W. G. Wier. 1992. Macroscopic and unitary properties of physiological ion flux through T-type Ca^{2+} channels in guinea-pig heart cells. *J. Physiol.* 456:247–265.

Barnes, S., and B. Hille. 1989. Ionic channels of the inner segment of tiger salamander cone photoreceptors. *J. Gen. Physiol.* 94:719–743.

Bean, B. P. 1985. Two kinds of calcium channels in canine atrial cells. *J. Gen. Physiol.* 86:1–30.

Charlton, M. P., and G. J. Augustine. 1990. Classification of presynaptic calcium channels at the squid giant synapse: neither T-, L- nor N-type. *Brain Res.* 525:133–139.

Corey, D. P., J. M. Dubinsky, and E. A. Schwartz. 1984. The calcium current in inner segments of rods from the salamander (*Ambystoma tigrinum*) retina. *J. Physiol.* 354:557–575.

Crawford, A. C., and R. Fettiplace. 1980. The frequency selectivity of auditory nerve fibres and hair cells in the cochlea of the turtle. *J. Physiol.* 312:377–412.

Crawford, A. C., and R. Fettiplace. 1981. An electrical tuning mechanism in turtle cochlear hair cells. *J. Physiol.* 312:377–412.

Davis, H. 1985. An active process in cochlear mechanics. *Hearing Res.* 9:79–90.

Fenwick, E. M., A. Marty, and E. Neher. 1982. Sodium and calcium channels in bovine chromaffin cells. *J. Physiol.* 331:599–635.

Fischer, F. P. 1992. Quantitative analysis of the innervation of the chicken basilar papilla. *Hearing Res.* 61:167–178.

Fox, A. P., M. C. Nowycky, and R. W. Tsien. 1987. Kinetic and pharmacological properties distinguishing three types of calcium currents in chick sensory neurones. *J. Physiol.* 394:149–172.

Fuchs, P. A., and M. G. Evans. 1990. Potassium currents in hair cells isolated from the cochlea of the chick. *J. Physiol.* 429:529–551.

Fuchs, P. A., M. G. Evans, and B. W. Murrow. 1990. Calcium currents in hair cells isolated from the cochlea of the chick. *J. Physiol.* 429: 553–568.

Fuchs, P. A., and K. A. Fagan. 1993. Calcium current magnitude correlates with presynaptic function in chick cochlear hair cells. *Annu. Meeting Soc. Neurosci.* 23:1076. (Abstr.)

Fuchs, P. A., and B. W. Murrow. 1992a. Cholinergic inhibition of short (outer) hair cells of the chick's cochlea. *J. Neurosci.* 12:800–809.

Fuchs, P. A., and B. W. Murrow. 1992b. A novel cholinergic receptor mediates inhibition of chick cochlear hair cells. *Proc. R. Soc. Lond. B.* 248: 35–40.

Fuchs, P. A., T. Nagai, and M. G. Evans. 1988. Electrical tuning in hair cells isolated from the chick cochlea. *J. Neurosci.* 8:2460–2467.

Hirokawa, N. 1978. The ultrastructure of the basilar papilla of the chick. *J. Comp. Neurol.* 181:361–374.

Hodgkin, A. L., and A. F. Huxley. 1952. A quantitative description of membrane current and its application to conduction and excitation in nerve. *J. Physiol.* 117:500–544.

Hudspeth, A. J., and R. S. Lewis. 1988a. Kinetic analysis of voltage- and ion-dependent conductances in saccular hair cells of the bull-frog, *Rana catesbeiana. J. Physiol.* 400:237–274.

Hudspeth, A. J., and R. S. Lewis. 1988b. A model for electrical resonance and frequency tuning in saccular hair cells of the bull-frog, *Rana catesbeiana. J. Physiol.* 400:275–297.

Leung, A. T., T. Imagawa, and K. P. Campbell. 1987. Structural characterization of the 1,4-dihydropyridine receptor of the voltage-dependent Ca^{2+} channel from rabbit skeletal muscle. *J. Biol. Chem.* 262:7943–7946.

Lewis, R. S., and A. J. Hudspeth. 1983. Voltage- and ion-dependent conductances in solitary vertebrate hair cells. *Nature.* 304:538–541.

Lewis, E. R., E. L. Leverenz, and W. S. Bialek. 1985. The Vertebrate Inner Ear. CRC Press, Boca Raton. 110–113.

Llinás, R., I. Z. Steinberg, and K. Walton. 1981. Presynaptic calcium currents in squid giant synapse. *Biophys. J.* 33:289–322.

Ma, J., L. M. Gutiérrez, M. M. Hosey, and E. Ríos. 1992. Dihydropyridine-sensitive skeletal muscle Ca channels in polarized planar bilayers. 3. Effects of phosphorylation by protein kinase C. *Biophys. J.* 63:639–647.

Manley, G. A. 1979. Preferred intervals in the spontaneous activity of primary auditory neurons. *Naturwissenschaften.* 66:582.

Manley, G. A., O. Gleich, H.-J. Leppelsack, and H. Oeckinghaus. 1985. Activity patterns of cochlear ganglion neurones in the starling. *J. Comp. Physiol.* 157:161–181.

Markwardt, F., and B. Nilius. 1988. Modulation of calcium channel currents in guinea-pig single ventricular heart cells by the dihydropyridine BAY K 8644. *J. Physiol.* 399:559–575.

Mikami, A., K. Imoto, T. Tanabe, T. Niidome, Y. Mori, H. Takeshima, S. Narumiya, and S. Numa. 1989. Primary structure and functional expression of the cardiac dihydropyridine-sensitive calcium channel. *Nature.* 340:230–233.

Mintz, I. M., V. J. Venema, K. M. Swiderek, T. J. Lee, B. P. Bean, and M. E. Adams. 1992. P-type calcium channels blocked by the spider toxin ω-Aga-IVA. *Nature.* 355:827–829.

Mundiña-Weilenmann, C., J. Ma, E. Ríos, and M. M. Hosey. 1991. Dihydropyridine-sensitive skeletal muscle Ca channels in polarized planar bilayers. 2. Effects of phosphorylation by cAMP-dependent protein kinase. *Biophys. J.* 60:902–909.

Navaratnam, D. S., and J. C. Oberholtzer. 1994. Molecular cloning of potassium channels from the chick cochlea. *Midwinter Res. Meeting Assoc. Res. Otolaryngol.* 17:139. (Abstr.)

Nowycky, M. C., A. P. Fox, and R. W. Tsien. 1985. Three types of neuronal calcium channel with different calcium agonist sensitivity. *Nature.* 316: 440–443.

Ohmori, H. 1984. Studies of ionic currents in the isolated vestibular hair cell of the chick. *J. Physiol.* 350:561–581.

Ono, K., and H. A. Fozzard. 1992. Phosphorylation restores activity of L-type calcium channels after rundown in inside-out patches from rabbit cardiac cells. *J. Physiol.* 454:673–688.

Pitchford, S., and J. F. Ashmore. 1987. An electrical resonance in hair cells of the amphibian papilla of the frog *Rana temporaria. Hearing Res.* 27:75–83.

Prigioni, I., S. Masetto, G. Russo, and V. Taglietti. 1992. Calcium currents in solitary hair cells isolated from frog crista ampullaris. *J. Vestib. Res.* 2:31–39.

Regan, L. J. 1991. Voltage-dependent calcium currents in Purkinje cells from rat cerebellar vermis. *J. Neurosci.* 11:2259–2269.

Regan, L. J., D. W. Y. Sah, and B. P. Bean. 1991. Ca^{2+} channels in rat central and peripheral neurons: high-threshold current resistant to dihydropyridine blockers and ω-conotoxin. *Neuron.* 6:269–280.

Reuter, H., and H. Scholz. 1977. A study of the ion selectivity and the kinetic properties of the calcium dependent slow inward current in mammalian cardiac muscle. *J. Physiol.* 264:17–47.

Roberts, W. M., R. A. Jacobs, and A. J. Hudspeth. 1990. Colocalization of ion channels involved in frequency selectivity and synaptic transmission at presynaptic active zones of hair cells. *J. Neurosci.* 10:3664–3684.

Robitaille, R., M. L. Garcia, G. J. Kaczorowski, and M. P. Charlton. 1993. Functional colocalization of calcium and calcium-gated potassium channels in control of transmitter release. *Neuron.* 11:645–655.

Rose, W. C., C. W. Balke, W. G. Wier, and E. Marban. 1992. Macroscopic and unitary properties of physiological flux through L-type Ca^{2+} channels in guinea-pig heart cells. *J. Physiol.* 456:256–284.

Sánchez, J. A., and E. Stefani. 1978. Inward calcium current in twitch muscle fibres of the frog. *J. Physiol.* 283:197–209.

Sánchez, J. A., and E. Stefani. 1983. Kinetic properties of calcium channels of twitch muscle fibres of the frog. *J. Physiol.* 337:1–17.

Schermuly, L., and R. Klinke 1985. Change of characteristic frequency of pigeon primary auditory afferents with temperature. *J. Comp. Physiol.* 156:209–211.

Spoendlin, H. 1972. Innervation densities of the cochlea. *Acta Otolaryngol.* 73:235–248.

Takahashi, M., M. J. Seagar, J. F. Jones, B. F. X . Reber, and W. A. Catterall. 1987. Subunit structure of dihydropyridine-sensitive calcium channels from skeletal muscle. *Proc. Natl. Acad. Sci. USA.* 84:5478–5482.

Takasaka, T., and C. A. Smith. 1971. The structure and innervation of the pigeon's basilar papilla. *J. Ultrastruct. Res.* 35:20–65.

Tanabe, T., H. Takeshima, A. Mikami, V. Flockerzi, H. Takahashi, K. Kangawa, M. Kojima, H. Matsuo, T. Hirose, and S. Numa. 1987. Primary structure of the receptor for calcium channel blockers from skeletal muscle. *Nature.* 328:313–318.

Tanaka, K., and C. A. Smith. 1978. Structure of the chicken's inner ear: SEM and TEM study. *Am. J. Anat.* 153:251–272.

Taylor, W. R. 1988. Two-suction-electrode voltage-clamp analysis of the sustained calcium current in cat sensory neurones. *J. Physiol.* 407:405–432.

Yue, D. T., S. Herzog, and E. Marban. 1990. β-Adrenergic stimulation of calcium channels occurs by potentiation of high-activity gating modes. *Proc. Natl. Acad. Sci. USA.* 87:753–757.

Zidanic, M., and P. A. Fuchs. 1993. Calcium currents in tall and short hair cells of the chick basilar papilla. *Midwinter Res. Meeting Assoc. Res. Otolaryngol.* 16:80. (Abstr.)